PNAS INAUGURAL ARTICLE | BIOCHEMISTRY CHEMISTRY

Pyruvate formate-lyase activating enzyme: The catalytically active 5′-deoxyadenosyl radical caught in the act of H-atom abstraction

Maike N. Lundahl[a], Hao Yang[b], William E. Broderick[a], Brian M. Hoffman[b], and Joan B. Broderick[a,1]

This contribution is part of the special series of Inaugural Articles by members of the National Academy of Sciences elected in 2022.
Contributed by Joan B. Broderick; received August 24, 2023; accepted October 3, 2023; reviewed by Sean J. Elliott and JoAnne Stubbe

Enzymes of the radical *S*-adenosyl-L-methionine (radical SAM, RS) superfamily, the largest in nature, catalyze remarkably diverse reactions initiated by H-atom abstraction. Glycyl radical enzyme activating enzymes (GRE-AEs) are a growing class of RS enzymes that generate the catalytically essential glycyl radical of GREs, which in turn catalyze essential reactions in anaerobic metabolism. Here, we probe the reaction of the GRE-AE pyruvate formate-lyase activating enzyme (PFL-AE) with the peptide substrate RVSG$_{734}$YAV, which mimics the site of glycyl radical formation on the native substrate, pyruvate formate-lyase. Time-resolved freeze-quench electron paramagnetic resonance spectroscopy shows that at short mixing times reduced PFL-AE + SAM reacts with RVSG$_{734}$YAV to form the central organometallic intermediate, Ω, in which the adenosyl 5′C is covalently bound to the unique iron of the [4Fe–4S] cluster. Freeze-trapping the reaction at longer times reveals the formation of the peptide G$_{734}$• glycyl radical product. Of central importance, freeze-quenching at intermediate times reveals that the conversion of Ω to peptide glycyl radical is not concerted. Instead, homolysis of the Ω Fe–C5′ bond generates the nominally "free" 5′-dAdo• radical, which is captured here by freeze-trapping. During cryoannealing at 77 K, the 5′-dAdo• directly abstracts an H-atom from the peptide to generate the G$_{734}$• peptide radical trapped in the PFL-AE active site. These observations reveal the 5′-dAdo• radical to be a well-defined intermediate, caught in the act of substrate H-atom abstraction, providing new insights into the mechanistic steps of radical initiation by RS enzymes.

S-adenosyl-L-methionine | 5′-deoxyadenosyl | radical | EPR | peptide

Significance

The radical *S*-adenosyl-L-methionine (SAM) enzyme superfamily, thought to be the largest in nature, catalyzes remarkably diverse and challenging reactions across all life's kingdoms. These reactions are initiated by H-atom abstraction from substrate at an active-site SAM-bound [4Fe–4S] cluster. Here, we provide snapshots of sequential radical intermediates during activation of a glycyl radical enzyme peptide mimic by its radical SAM activating enzyme, which catch the elusive 5′-dAdo• intermediate in the act of directly carrying out H-atom abstraction from the substrate.

The involvement of organic radicals in biological catalysis, once a controversial proposal, is now broadly accepted: (1–3) Radical reactions are central to enzymatic catalysis and in large part are carried out by what is thought to be the largest enzyme superfamily in Nature, the radical *S*-adenosyl-L-methionine (SAM) superfamily (4, 5). The radical SAM (RS) superfamily spans all kingdoms of life and exhibits remarkable functional diversity across even the small fraction of superfamily members that have been characterized to date (6–11). Despite this breadth and diversity of reactions catalyzed, RS enzymes share common structural features, in particular a conserved cysteine motif (CX_3CX_2C or variations) that binds three irons of a [4Fe–4S] cluster, with the fourth iron serving as the site of coordination of SAM (12–15). This fundamental architecture serves as the starting point for radical initiation across the superfamily (16–18).

Among the founding members of the RS superfamily are pyruvate formate-lyase activating enzyme (PFL-AE) and the anaerobic ribonucleotide reductase activating enzyme, two examples of the growing class of glycyl radical enzyme activating enzymes (GRE-AEs) that activate GREs, (19) which in turn catalyze essential reactions in anaerobic metabolism (20–24). PFL-AE catalyzes the post-translational installation of a catalytically essential glycyl radical on the glycyl radical enzyme PFL, (25) which uses this radical to initiate the conversion of pyruvate to acetyl-CoA and formate under anaerobic conditions, the equivalent of the pyruvate dehydrogenase reaction in aerobic organisms (26). In seminal work beginning nearly 50 y ago, Knappe and coworkers demonstrated the dependence of PFL activation on SAM, (27) and identified PFL-AE as the activating enzyme that abstracts the Cα pro-*S* H-atom at PFL G734 to form the glycyl radical cofactor of active PFL (Fig. 1) (25, 28, 29). The PFL G734• radical is stable for many hours under anaerobic conditions; (30) this stability is attributed to the fact that the G734 loop of PFL is buried in the interior of the protein and thus protected from quenching by solvent components (31, 32). Exposure to oxygen damages active PFL-G734•, but its activity can be restored by a "spare part" protein that replaces the glycyl radical domain and provides its own glycyl residue capable of undergoing activation by PFL-AE (33–35).

Author affiliations: [a]Department of Chemistry and Biochemistry, Montana State University, Bozeman, MT 59717; and [b]Department of Chemistry, Northwestern University, Evanston, IL 60208

Author contributions: W.E.B. and J.B.B. designed research; M.N.L. and H.Y. performed research; M.N.L., H.Y., W.E.B., B.M.H., and J.B.B. analyzed data; B.M.H. and J.B.B. acquired funding; and M.N.L., W.E.B., B.M.H., and J.B.B. wrote the paper.

Reviewers: S.J.E., Boston University; and J.S., Massachusetts Institute of Technology.

The authors declare no competing interest.

[1]To whom correspondence may be addressed. Email: jbroderick@montana.edu.

This article contains supporting information online at https://www.pnas.org/lookup/suppl/doi:10.1073/pnas.2314696120/-/DCSupplemental.

Published November 13, 2023.

The buried location of the PFL G734• radical, together with the evidence for PFL-AE catalyzed direct H-atom abstraction from PFL G734, hints at major structural rearrangements of PFL in order to bind the glycyl radical loop in the PFL-AE active site (11, 32). A simpler model of the large 170 kDa PFL substrate was introduced by Knappe and coworkers, who showed that short peptides that replicate the sequence surrounding PFL G734 (in particular the seven-mer peptide RVSG$_{734}$YAV, denoted G-pep) serve as substrate analogs that, like PFL, stimulate the reductive cleavage of SAM by PFL-AE (29). These peptide substrate mimics also provided the first direct evidence for the stereochemistry of H-atom abstraction during GRE activation (29). More recently, X-ray structural determination by Drennan and coworkers of the ternary complex of PFL-AE with both SAM and the synthetic G-pep peptide mimic of the PFL substrate bound in the active site provided key insights into the structural basis for glycyl radical enzyme activation (36, 37). However, although, these short peptides thus have provided key mechanistic and structural insights, the inferred peptide radical products were not observed, presumably due to the lack of a protective PFL protein pocket to protect them from quenching.

RS chemistry such as that involved in the activation of PFL by PFL-AE is proposed to proceed by initial electron transfer from the reduced $[4Fe–4S]^{+}$ cluster to the sulfonium of SAM, leading to homolytic S-C5′ bond cleavage to form a 5′-deoxyadenosyl radical (5′-dAdo•) that ultimately abstracts a hydrogen atom from substrate (Fig. 1) (6, 7, 38–41). Efforts to understand the mechanistic details of this process in the PFL-AE/PFL reaction led to the discovery of an organometallic intermediate, Ω, in which the adenosyl moiety formed by homolytic cleavage of the SAM S-C5′ bond is covalently bound by its 5′C to the unique iron of the [4Fe–4S] cluster (42, 43). Thermal annealing experiments showed Ω is a functional intermediate in the process of PFL H-atom abstraction (42). The observation that Ω is formed in a wide range of RS enzymes further showed it to be a central catalytic intermediate throughout the superfamily (16, 17, 44–47).

The Ω intermediate is remarkably similar to coenzyme B_{12} (adenosylcobalamin) in that both are organometallic complexes that generate 5′-dAdo• by cleavage of a bond between the C5′ atom of the adenosyl group and a metal ion: Co(III) in B_{12} and the unique Fe of the $[4Fe–4S]^{3+}$ cluster in Ω (16). The 5′-dAdo• radical is central to catalysis in both B_{12} and RS enzymes as it carries out the substrate H-atom abstraction that initiates subsequent chemistry, (17) but over half a century of efforts to capture and characterize this highly reactive primary radical were fruitless. In particular, early work revealed that photolysis of

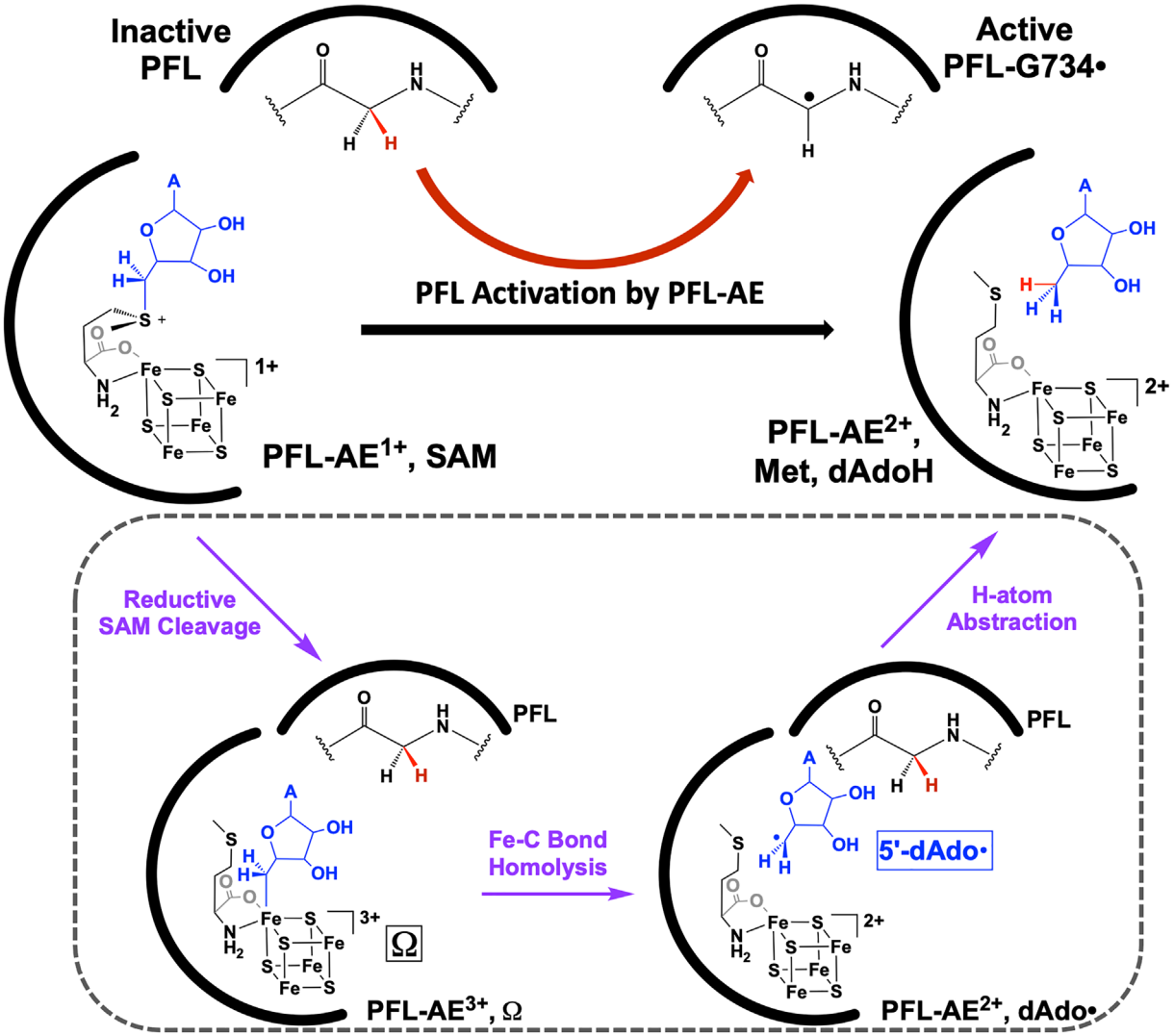

Fig. 1. PFL-AE catalyzed activation of PFL via the fundamental radical initiation steps proposed to be shared by all RS enzymes. (*Top*) overall reaction for the activation of PFL by PFL-AE. *Bottom* inside dashed box, proposed mechanistic steps including the formation of the organometallic intermediate Ω, liberation of 5′-dAdo• via Fe–C bond homolysis, and stereospecific hydrogen atom abstraction from the G734 of PFL. "A" denotes an adenine moiety.

adenosylcobalamin led to Co–C bond homolysis, but efforts to characterize the resulting 5′-dAdo• were thwarted by the effects of spin-coupling to the nearby paramagnetic Co(II)-cobalamin (48). Only recently was it discovered that cryo-photolysis of the $[4Fe–4S]^{+}$/SAM complex of PFL-AE induced electron transfer from the $[4Fe–4S]^{+}$ cluster to the sulfonium group of SAM, resulting in S-C5′ bond homolysis to generate the 5′-dAdo• radical (49). Subsequently, photolysis of diverse RS enzymes revealed that all undergo photoinduced reductive cleavage of SAM, with some forming the 5′-dAdo• and others cleaving the SAM S-CH_3 bond to form a •CH_3 radical (50). These results led to a new understanding of the origins of regioselectivity during reductive cleavage of SAM, both photochemical and enzymatic (51, 52).

This photoinduced electron transfer process enabled the first capture and characterization of the 5′-dAdo• radical (49). The use of SAM isotopologs showed that the distinctive EPR (electron paramagnetic resonance) signal of the 5′-dAdo• is dominated by α-hyperfine coupling of the spin localized in the 2pπ orbital on C5′ to the 5′-H atoms, β-coupling to the 4′-H, and a characteristically large ^{13}C5′ hyperfine coupling (49). In other work, use of a substrate analog with an increased barrier to hydrogen atom abstraction enabled observation this 5′-dAdo• radical in the RS enzyme HydG under nonturnover conditions (53). The first unequivocal evidence for a catalytically competent "free" 5′-dAdo• radical during catalysis was provided through detailed examination of a nonnative adenosylation reaction catalyzed by PFL-AE with a dehydroalanine-containing peptide as substrate analog (54).

Here, we examine mechanistic details of the PFL-AE catalyzed reaction with the G-pep 7-mer peptide model of the 170 kDa PFL substrate protein. Time-resolved freeze-quench EPR experiments show that the PFL-AE/SAM complex binds G-pep and reacts to form the central organometallic intermediate Ω, which was first seen with the reaction of PFL-AE with PFL, and that has been widely observed for RS enzymes reacting with their native substrates (42, 44). Freeze-trapping the reaction with G-pep at longer times reveals the formation of the G-pep glycyl radical (G-pep•), as unequivocally identified through EPR spectroscopy combined with isotopic labeling and density functional theory (DFT) calculations. Of central importance, samples freeze-quenched at intermediate times revealed not only the G-pep• glycyl radical, but also the presence of the elusive 5′-dAdo• radical generated upon homolytic cleavage of Ω during enzymatic turnover. Upon extended 77 K cryoannealing, EPR spectroscopy showed that the 5′-dAdo• radical thus formed converts to the G-pep• radical, demonstrating that the 5′-dAdo• radical is indeed the reactive catalytic intermediate—caught in the act of H-atom abstraction.

Results

Trapping the Organometallic Intermediate Ω During Reaction of PFL-AE, SAM and G-pep. RFQ (Rapid freeze-quench) EPR measurements were carried out over a range of short delay times of ~1 s and less, to probe the initial steps in the reaction of PFL-AE with SAM and G-pep (Scheme 1). Spectra collected on samples quenched at 500 ms and 1 s exhibit the signal of the organometallic intermediate Ω ($g_{\|}$ = 2.036 and $g_{\perp}$ = 2.004) with

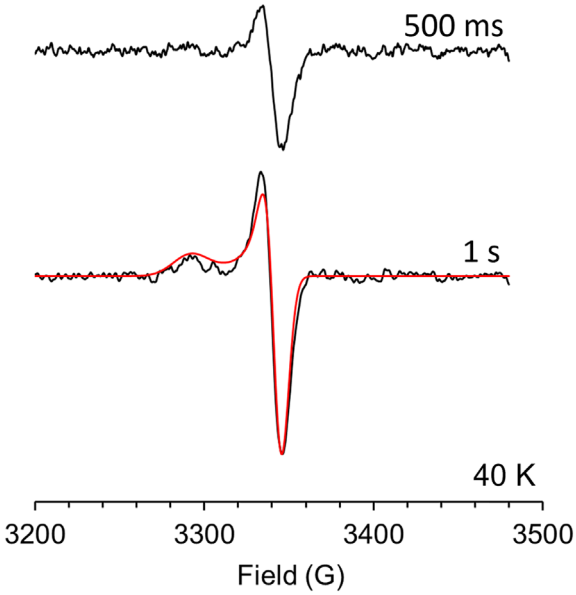

Fig. 2. EPR spectra of the PFL-AE/SAM/G-pep reaction quenched at 500 ms and 1 s reveals formation of Ω. RFQ at 500 ms (*Top*) and 1 s (*Bottom*) shows an EPR signal characteristic of Ω (black). Conditions: Rapid freeze-quenched, 500 ms and 1.0 s; frequency, 9.376 GHz; modulation, 10 G; T = 40 K. Simulation (red) generated with Easyspin (55) using $g_{\|}$ = 2.036 and $g_{\perp}$ = 2.004 and linewidth parameter 0.75.

the signal at the later time having greater intensity (Fig. 2) (42). The observation of Ω during the reaction of reduced PFL-AE with SAM and G-pep thus demonstrates that this small 7-mer peptide is able to initiate SAM cleavage with Ω formation in an analogous manner to the large 170 kDa native PFL substrate.

The expected reaction progress would ultimately involve subsequent H-atom abstraction from the G734 residue of G-pep by 5′-dAdo•. However, when Ω formed during reaction of PFL-AE, SAM, and G-pep is sequentially annealed at temperatures of 150 K for 1 min,180 K for 1 min, then 220 K for 3 min the Ω EPR signal is greatly decreased without detectable appearance of a signal attributable to a glycyl radical (*SI Appendix*, Fig. S2). This is in contrast to the reaction of Ω formed with the PFL enzyme as substrate, which was shown to yield the PFL G734• radical during annealing (42).

The inability to observe the G-pep• product radical during cryoannealing of freeze-trapped Ω (*SI Appendix*, Fig. S2) likely indicates that the trapped conformation of the bound peptide precursor somehow prevents the pro-*S* H-atom from reacting with 5′-dAdo• liberated by Ω, with the radical instead undergoing solvent quenching. It is also possible the peptide glycyl radical forms but is quenched and does not build up to observable levels. In order to observe radical species subsequent to Ω, we pursued time-resolved freeze-quench experiments at longer reaction times, as discussed in the following sections.

Peptide Glycyl Radical Revealed by Freeze-Quench at ~10 s. When reduced PFL-AE was reacted with SAM and G-pep at ambient temperature for ~8 to 10 s and then freeze-quenched in liquid nitrogen, the EPR spectrum collected at 70 K is the

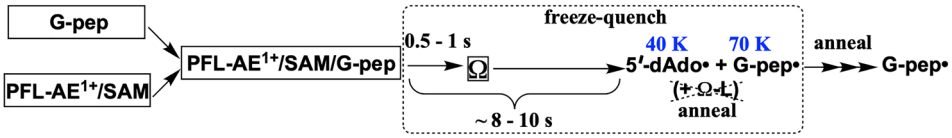

Scheme 1. Schematic description of the mixing (*Left*), freeze-quench (*Middle*), and annealing (*Right*) techniques used to trap sequential radical species.

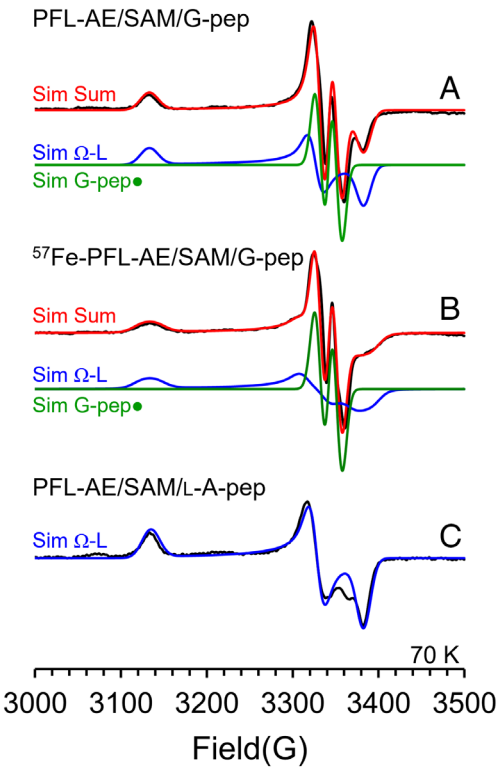

Fig. 3. EPR spectra of the reaction of reduced PFL-AE, SAM and G-pep quenched at ~8 to 10 s reveals the presence of Ω-L in addition to the G-pep glycyl radical, while A-pep gives only Ω-L. (*A*) Reaction using SAM and natural abundance PFL-AE with G-pep. (*B*) Reaction using SAM and ^{57}Fe- PFL-AE with G-pep. (*C*) Reaction using SAM and PFL-AE with L-A-pep. The simulations (red, blue and green) were generated with Easyspin (55) using parameters for G-pep• listed in Table 1, and the following parameters for Ω-L: g = [2.137, 2.0125, 1.979], g strain [0.0142, 0.007, 0.008, and linewidth 1.2. For simulation in *B*, ^{57}Fe couplings, A = 50 MHz. EPR conditions: microwave frequency, 9.38 GHz; modulation, 3 G, T = 70 K.

superposition of signals from two paramagnetic species. One is the peptide glycyl radical product, with g_{iso} = 2.004 and hyperfine splitting by a single ^{1}H with a_{iso} = 52 MHz. The second is an Ω-like species (denoted Ω-L), without resolved hyperfine and an anisotropic g-tensor, g = [2.137, 2.013, 1.978] (Fig. 3) whose g-symmetry/anisotropy is similar to that of the organometallic Ω intermediate, $g_{\|}$ = 2.035 and $g_{\perp}$ = 2.004 (42, 44, 46, 50, 52, 56, 57). To confirm the identification of the Ω-L signal as associated with a 5′-dAdo-bound cluster, an Ω center with spin localized on the [4Fe–4S] cluster, we carried out EPR experiments with ^{57}Fe-enriched PFL-AE. ^{57}Fe-labeling does not affect the EPR linewidth of the glycyl radical signal, but it broadens the rhombic g_{ave} > 2 signal of Ω-L (Fig. 3) by an amount comparable to the ^{57}Fe broadening of Ω, as expected for the identification of Ω-L as an organometallic complex of an $[4Fe–4S]^{3+}$ cluster with bound 5′-dAdo. The difference in g-tensors between Ω and Ω-L presumably is associated with a somewhat modified conformation for Ω-L. This difference is compatible with the idea that formation of Ω-L during the extended reaction time of 8 s at ambient temperatures allows access to a range of conformations unavailable during the short-time RFQ.

Previously, we showed that the modified enzyme, PFL G734A, also triggers SAM cleavage by PFL-AE and formation of Ω during rapid RFQ, but that the replacement of the pro-*S* H-atom of G734 with the -CH_3 side chain of alanine prevented formation a protein radical (42). Here, we correspondingly carried out 8 to 10 s freeze-quench reactions with the analogous G-pep variant in which the central G734 glycyl residue is replaced with L-alanine (L-A-pep). Reaction of reduced PFL-AE with SAM and L-A-pep for ~10 s prior to freeze-quenching generates an Ω-L cluster-based signal with a g-tensor, $\boldsymbol{g}$ = [2.137, 2.013, 1.978], similar to that observed in the G-pep reaction (Fig. 3 and *SI Appendix*, Fig. S3).

Characterization of the G-pep Glycyl Radical. The Ω-L signal observed in the 8-s reaction of PFL-AE with SAM and G-pep is stable upon annealing at 180 K, but is lost upon annealing at 220 K without converting into a new radical signal (*SI Appendix*, Fig. S4). The properties of Ω-L and its possible role in catalysis are currently under investigation. However, this annealing procedure allowed the monitoring of a clean signal from the glycyl radical, which persists upon 220 K annealing. Thus, a sample of reduced PFL-AE with SAM and G-pep freeze-quenched in liquid nitrogen ~8 to 10 s after mixing was annealed at 220 K for 5 min to remove contributions from Ω-L and then examined by EPR spectroscopy at 70 K (Fig. 4). The resulting signal is indeed characteristic of a glycyl radical: centered at g_{iso} = 2.004 with a ^{1}H doublet arising from hyperfine coupling to the G734• Cα–H, with splitting, a_{iso} = 52 MHz. This signal is similar to other characterized glycyl radicals, including that in activated PFL, but the hyperfine coupling for G-pep• glycyl radical is larger than the 42 MHz observed for the PFL glycyl radical (25). This indicates that the G-pep• glycyl radical has a somewhat altered structure; this will be addressed in more detail in the following section.

A sample of G-pep• prepared as just described, but in D_2O rather than H_2O, exhibits a sharpened G-pep• glycyl radical ^{1}Hα doublet, Fig. 4, indicative of the presence of a weaker hyperfine coupling to an exchangeable ^{1}H that is lost in D_2O. Simulation of the spectrum in Fig. 4 gives $a_{iso} \cong$ 10 MHz for this weaker coupling lost in D_2O, which is assignable to the adjacent amide N–H. The reaction carried out in D_2O also provides greater EPR

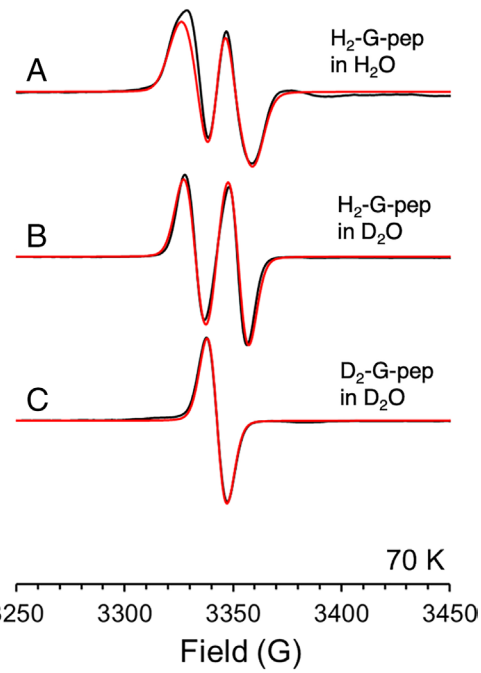

Fig. 4. EPR analysis of the G-pep radical from reactions quenched at ~10 s: normalized X-band EPR spectra (black) generated from the reaction of reduced PFL-AE, SAM and G-pep freeze quenched at ~8 to 10 s and annealed at 220 K for 5 min to remove Ω-L, overlaid with simulations of G-pep• signals using parameters listed in Table 1 (red). (*A*) Reaction using SAM and natural abundance Gly-pep. (*B*) Reaction using SAM and natural abundance Gly-pep carried out in 95% D_2O. (*C*) Reaction using SAM and D_2-Gly-pep carried out in 95% D_2O. The simulations(red) were generated with Easyspin (55) EPR conditions: microwave frequency, 9.38 GHz; modulation, 3 G, T = 70 K.

signal intensity for the G-pep• glycyl radical (*SI Appendix*, Fig. S5), indicating that D_2O slows solvent quenching of either G-pep• or the 5′-dAdo• active species that generates this radical, as a result of the H/D isotope effect, and thereby enhances the product-radical buildup.

To further examine the formation of the G-pep• glycyl radical, reaction of reduced PFL-AE with SAM and peptide was carried out in H_2O with glycine-Hα deuterated peptide (D_2-G-pep). Surprisingly, this procedure did not produce appreciable amounts of G-pep• signal (*SI Appendix*, Fig. S6). However, when the PFL-AE/SAM/D_2-G-pep reaction was carried out in 95 % D_2O, the resulting sample exhibited an EPR signal in which the doublet had collapsed, unequivocally demonstrating the formation of the G-pep• glycyl radical, deuterated at Cα (Fig. 4 and *SI Appendix*, Fig. S6). Our interpretation of these results is that the H/D isotope effect slows reaction of 5′-dAdo• with D_2-G-pep, and that as a result G-pep• radical formation cannot compete with solvent quenching of 5′-dAdo• and/or G-pep• by H_2O. However, when the D_2-G-pep reaction is carried out in D_2O, solvent quenching also is slowed, allowing accumulation of the D-G-pep• product radical with its singlet EPR signal.

Ambient-temperature reaction with even longer quench times yields decreasing quantities of the G-pep• EPR signal (*SI Appendix*, Fig. S7), a decrease that is particularly pronounced in the presence of DTT, where even short quench times provide no detectable G-pep• (*SI Appendix*, Fig. S8). This contrasts with the stoichiometric accumulation of G734• PFL during reaction of PFL-AE with PFL, in a process that is not negatively impacted by DTT (38). The loss of G-pep• with increasing reaction time or with the presence of dithiothreitol (DTT) is attributed to quenching of the relatively solvent-exposed and unprotected peptide glycyl radical, a situation very different than that of the G734• of PFL, which is buried within the interior of the large PFL protein (31).

Structure of the G-pep Glycyl Radical. The increased Cα–H hyperfine coupling (52 MHz) for the G-pep• glycyl radical relative to the 42 MHz observed for the PFL glycyl radical (25) suggests that the structures of the two radicals differ slightly. X-ray crystallography has revealed the structure of the nonradical state of PFL G734 (31) and the structure of nonradical G-pep bound in the PFL-AE active site (36). There are no corresponding crystallographic measurements for the radical states of PFL and G-pep, but both computational and high-field EPR studies indicate that the hyperfine couplings observed for PFL G734• are consistent with a planar conformation, with a dihedral angle, ψ, of ~ 90° between the Cα radical 2pπ orbital and the adjacent N–H bond (58, 59).

The fixed conformation defined by the X-ray crystal structure for G-pep bound in the PFL-AE active site (PDB: 3CB8) would impose a dihedral angle, ψ, of ~ 50° between the 2pπ orbital of a planar Cα radical and the adjacent NH bond. To evaluate whether the experimental data reported here are consistent with G-pep• bound in the PFL-AE active site in a conformation similar to that crystallographically determined for G-pep, and thus different from that in the planar radical form of PFL, we employed DFT calculations. A computational model of G-pep• was constructed by truncating the 7-mer G-pep at the Cα of Ser733 and the amide nitrogen of Tyr735 (5, *SI Appendix*, Fig. S1). This peptide fragment model was given a fixed conformation based on the crystallographically determined structure of G-pep bound in the PFL-AE active site (36). The geometry around the Cα of Gly734 was changed to a planar sp^2 radical configuration. The resulting conformation, with its dihedral angle, ψ, of ~ 50° between the Cα radical 2pπ orbital and the adjacent N–H bond, yields β-proton

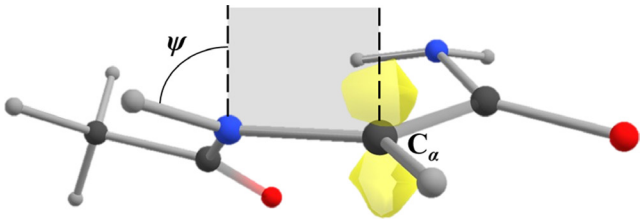

Fig. 5. Computational model of G-pep• with a dihedral angle $\psi \approx 60°$. The 2pπ radical orbital on the C_α is visualized in yellow.

hyperfine couplings even larger than the experimental values. However, only a slight rotation about the Cα–N bond to a dihedral angle of $\psi \approx 60°$ provided a model (Fig. 5) with both α and β couplings that agree well with the experimental data (Table 1). Together, our DFT calculations and experimental data support a model in which the G-pep• is held in a conformation similar to that crystallographically characterized for G-pep bound in the PFL-AE active site but distinct from that adopted by G734• in activated PFL (36). These results, together with earlier experimental and computational work, indicate that DFT combined with EPR spectroscopy can be useful in evaluating the conformation of protein glycyl radicals (58, 59).

Trapping of the 5′-dAdo• Radical

Although the ambient-temperature reaction of reduced PFL-AE, SAM, and G-pep quench-trapped at ~8 to 10 s gives a 70 K EPR spectrum dominated by the glycyl radical of G-pep• (Fig. 3), as the EPR observation temperature is reduced, a more complex signal gradually grows in (*SI Appendix*, Fig. S9). At 40 K, the EPR spectrum is dominated by a signal with features similar to those of 5′-dAdo•, which was previously observed upon photolysis of reduced PFL-AE/SAM in the absence of substrate (Fig. 6) (49). Inspection of the spectrum shown in Fig. 6 suggests that the G-pep glycyl radical signal is decreased but not completely suppressed at 40 K, consistent with the temperature dependence of the G-pep• glycyl radical signal (*SI Appendix*, Fig. S10). To remove residual G-pep• and Ω-L contributions from the 40 K EPR spectrum, a scaled subtraction of the 60 K spectrum (*SI Appendix*, Fig. S11) was carried out to generate the better-resolved 5′-dAdo• spectrum shown in Fig. 6. This spectrum was simulated with hyperfine parameters that correspond well to those previously reported for the 5′-dAdo• radical generated by photolysis (Table 2) (49). The identification of this signal as the 5′-dAdo• radical was unequivocally confirmed by use of isotopically labelled [adenosyl-5′,5″,4′,3′-D_4]-SAM during reaction with PFL-AE and G-pep, which resulted in collapse of the hyperfine-split pattern to a singlet, with minor contributions from an overlapping signal due to residual natural-abundance 5′-dAdo• (Fig. 6 and *SI Appendix*, Fig. S12). Given the above observation that the reaction of reduced PFL-AE with SAM and G-pep begins with the formation of an Ω species, we infer that the 5′-dAdo• being observed at long quench-time arises from homolysis of the Fe–C5′ bond of Ω.

Table 1. EPR simulation and DFT calculated parameters for the glycyl radical of G-pep•

G-pep•	Expl. Sim.	Calc.
g	2.0038 2.0033 2.003	2.0044 2.0034 2.0029
Cα-^{1}H (MHz)	−26, −80, −50	−22, −90, −57
N-^{1}H (MHz)	18, 25, 12	18, 30, 14
ψ	60°	60°

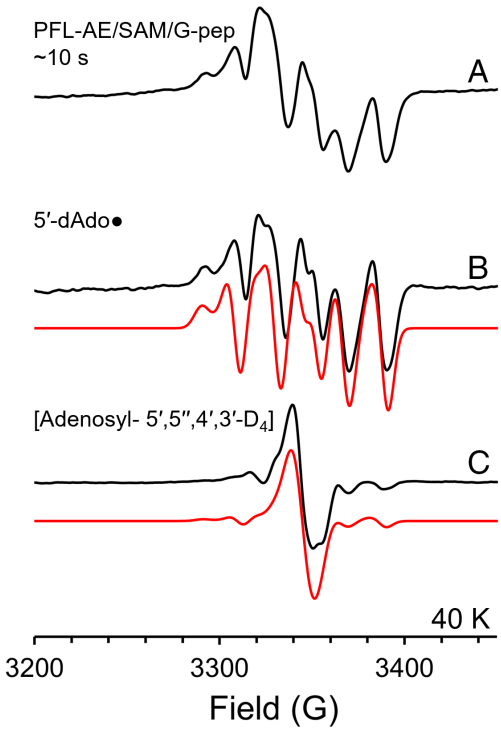

Fig. 6. EPR spectra of PFL-AE/SAM/G-pep reactions quenched at 10 s and then observed at 40 K reveal the presence of 5′-dAdo•. (*A*) Normalized X-band EPR spectrum (black) at 40 K generated from the reaction of reduced PFL-AE, SAM, and G-pep at RT then freeze-quenched at ~10 s. (*B*) Reaction using natural abundance SAM and Gly-pep with the 5′-dAdo• signal isolated by scaled subtraction of 60 K spectra. (*C*) Reaction using [adenosyl-5′,5″,4′,3′-D_4]-SAM and Gly-pep with contributions from the 5′-dAdo• signal isolated by scaled subtraction of 60 K spectra. The simulations (red) were generated with Easyspin (55) using parameters listed in Table 2. They incorporated 70% isotopically labelled and 30% natural abundance radical. EPR conditions: microwave frequency, 9.38 GHz; modulation, 3 G, T = 40 K.

The Trapped 5′-dAdo• Radical Carries Out H-Atom Abstraction. To evaluate whether the 5′-dAdo• observed in these experiments is a catalytically competent intermediate on pathway to H-atom abstraction from G-pep, the timecourse of this reaction was probed by examining with EPR spectroscopy samples annealed at 77 K for extended time periods and then at 220 K (Fig. 7 and *SI Appendix*, Figs. S13–S16). The spectra reveal progressive loss of the 5′-dAdo• signal (best visualized at 40 K) with accompanying appearance of the G-pep• signal (best visualized at 70 K), indicating that 5′-dAdo• converts to G-pep• upon cryo-annealing (Fig. 7). Quantitation of these changes reveal that between 1 and 10 d annealing at 77 K, the 5′-dAdo• radical population decreases by ~28% (from ~87 to ~59% of total radical population), while over the same period of cryoannealing, the G-pep• population increases by an equal amount (Fig. 7 and *SI Appendix*, Figs. S15 and S16 and Table S1). The remaining 5′-dAdo• quantitatively converted to the G-pep• radical when the sample was then annealed at 220 K for 5 min (Fig. 7 and *SI Appendix*, Figs. S13–S16). The total spin concentration in these experiments is low (~4 μM for 225 μM enzyme); we attribute this to the fact that 5′-dAdo• is a reactive radical intermediate that does not build up to high levels, and the G-pep• is short-lived due to solvent quenching. The total spin reported here for the G-pep reaction is approximately half that reported for the reaction of PFL-AE with a dehydroalanine-peptide substrate, where the resulting peptide radical is more stable and therefore easier to capture; in both studies the total spin concentration of 5′-dAdo• observed is similar at 3 to 4 μM (54). The clean conversion of the cryo-trapped 5′-dAdo• radical to the G-pep• radical demonstrates that this 5′-dAdo•, formed by homolysis of the Fe–C5′ bond of Ω, is a catalytically reactive intermediate, able to abstract an H-atom from substrate even in the frozen state.

Table 2. EPR simulation and DFT calculated parameters for the 5′-dAdo•

5′-dAdo•	Expl. Sim.	Photolysis (49)	Calc. (49)
5′-C-^{1} Hα_a	-15, -105, -50	-15, -105, -60	-28, -104, -63
(α, β, γ)	0, 120, 0	0, 120, 0	
5′-C-^{1} Hα_b	-20, -90, -50	-20, -95, -60	-25, -101, -61
(α, β, γ)	0, 0, 0	0, 0, 0	
4′-C-^{1} Hβ_a	+80, +85, +110	+80, +80, +110	+90, +90, +105
(α, β, γ)	40, 0, 0	40, 0, 0	

Discussion

PFL is a central enzyme in anaerobic glucose metabolism, catalyzing the conversion of pyruvate to acetyl-CoA and formate, and is the founding member of the increasingly important GRE family (21–24). Its activity is regulated in part by a posttranslational activation that was first recognized by Knappe and coworkers more than half a century ago (27, 60, 61). They showed that this activation involved installation of a catalytically essential free radical on the G734 residue of PFL by a specific activating enzyme, PFL-AE (25, 28, 62). The G734• radical on PFL was found to be a remarkably stable catalytic cofactor under anaerobic conditions, a stability attributed to the location of the glycyl-radical loop deep within the PFL protein structure, where it would be protected from nonspecific quenching (31). Peptides homologous to the PFL glycyl radical loop were found to stimulate the reductive cleavage of SAM by PFL-AE, indicating that they served the role of the PFL substrate but no evidence for formation of the unprotected, and thus, presumably less stable, peptide glycyl radicals was reported (29).

Here, we employed time-resolved freeze-quench and cryoannealing EPR techniques to probe the reaction of PFL-AE with peptide mimics of the native PFL substrate. We found that reaction of reduced PFL-AE with SAM and G-pep indeed rapidly induces SAM cleavage, and at reaction times of 0.5 to 1 s the reaction produces the Ω organometallic intermediate identical to that observed in the native reaction with PFL (42). Ω is a central intermediate during initiation of RS enzyme catalysis across the superfamily, (44) and so its observation in the reaction of PFL-AE with G-pep shows that the 7-mer peptide is a competent mimic of the native 170 kDa PFL substrate, capable of inducing the reductive cleavage reaction of SAM that leads to the initial formation of the organometallic intermediate Ω. It is remarkable that binding of such a small peptide substrate mimic can trigger the same radical-initiation chemistry as the much larger native PFL substrate. The ability of G-pep to initiate reductive cleavage of SAM and formation of Ω is consistent with the X-ray structure of the ternary complex of PFL-AE, SAM, and G-pep, where the close approach of the G734 Cα to the 5′C of SAM, and the SAM sulfur to the unique cluster Fe, reflects a system poised for stereospecific radical initiation (36).

Analysis of reduced PFL-AE/SAM/G-pep reactions quenched at longer reaction times of ~8 to 10 s reveals formation of an Ω conformer denoted Ω-L, as well as a glycyl radical on G-pep

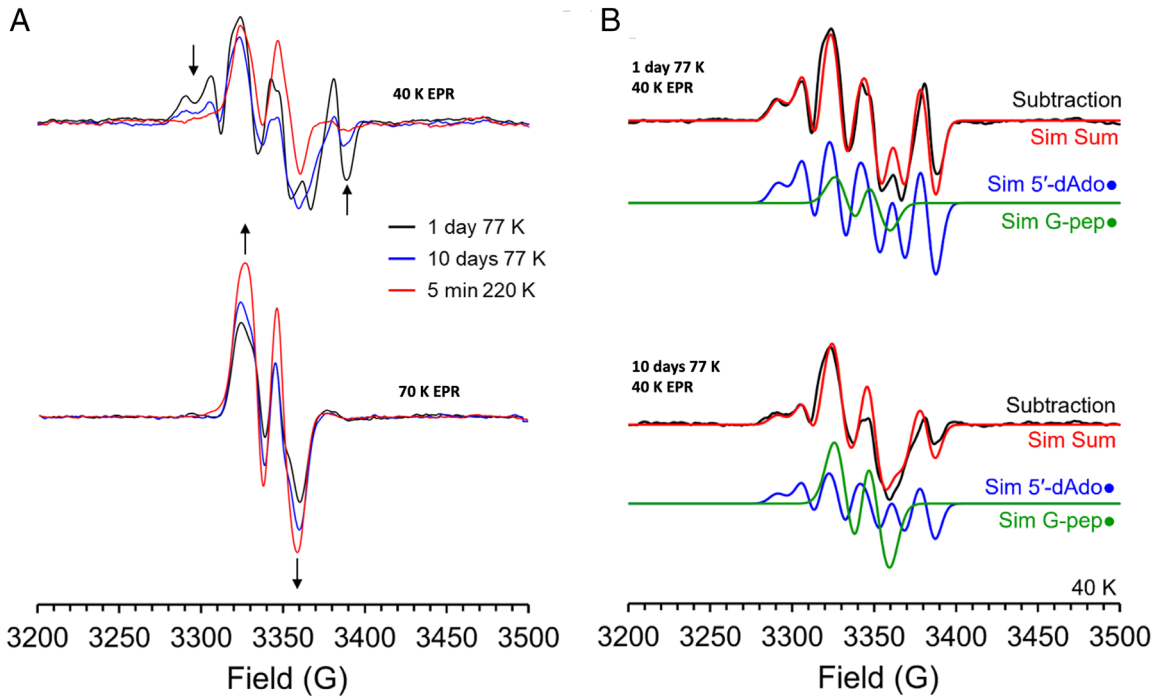

Fig. 7. EPR spectra of PFL-AE/SAM/G-pep reactions freeze-quenched at ~10 s reveal conversion of 5′-dAdo• to G-pep• upon cryo-annealing. (*A*) EPR spectra of the isolated organic radical signals generated in the 10 s quenched reaction of PFL-AE/SAM/G-pep with Ω-L removed via subtraction (See *SI Appendix* for additional details) recorded at 40 K (*Top*) have contributions from both 5′-dAdo• and G-pep• signals, while those at 70 K (*Bottom*) are dominated by the G-pep• signal. Cryo-annealing decreases intensity of the 5′-dAdo• signal while increasing intensity of the G-pep• signal (arrows). (*B*) Decomposition of contributing signals via simulation. (*Top*) The EPR spectrum observed after 1 d at 77 K (black) is simulated as the sum of 87 % 5′-dAdo• (blue) and 13% G-pep• (green). (*Bottom*) The EPR spectrum observed after annealing for 10 d at 77 K (black) is simulated as the sum of 59% 5′-dAdo• and 41% G-pep•. Simulations were generated with Easyspin (55) using a 5′-dAdo• model with parameters listed in Table 2 and a G-pep• with parameters listed in Table 1. EPR conditions: microwave frequency, 9.38 GHz; modulation, 3 G, T = 40 K or 70 K.

(Figs. 3 and 4); the formation of G-pep• demonstrates that the binding of the small G-pep indeed promotes H-atom abstraction from G734 in much the same way as occurs with the native substrate PFL, as previously suggested by Knappe (29). The G-pep• glycyl radical differs slightly from that of the well-characterized PFL G734• radical, with a somewhat larger hyperfine coupling to the Cα–^{1}H, a_{iso} = 52 MHz for G-pep• vs 42 MHz for PFL G734• (25). The larger coupling in G-pep• is attributed to a nonplanar conformation (ψ ~ 60°, Fig. 5) of the G-pep• radical bound to the PFL-AE active site that is similar to that observed in the PFL-AE/SAM/G-pep X-ray structure. This is different from that of the G734• buried in PFL, which is in a planar conformation (ψ ~ 90°) that would maximize π-delocalization and thus stabilization of the G734• radical. Indeed, computational and high-field EPR studies both agree that the G734• radical in PFL is planar, with the computational studies predicting the 42 MHz Cα-^{1}H coupling observed for G734•, (58, 59), whereas our DFT computations suggest that G-pep• radical in the current study is distorted (ψ ~ 60°) relative to the planar PFL G734•. This nonplanarity of G-pep• alters the hyperfine couplings and also makes the radical less stable due to the suboptimal conformation for full π-delocalization onto the adjacent amido and carboxy substituents, consistent with prior computational studies of a glycine dipeptide radical model (58). G-pep• bound in the PFL-AE active site is also a good model for the PFL G734• radical initially formed in the PFL-AE active site that would be expected to have a similar higher-energy conformation as observed here for G-pep•.

The stabilization achieved by converting the initially distorted higher energy PFL G734• radical to the more stable planar G734• radical buried in the PFL active site could thus help drive the large-scale structural rearrangements that occur during the later stages of PFL activation: movement of the PFL glycyl radical loop out of the PFL-AE active site and back into its buried location within PFL (32, 35, 36, 63). In the present study, we were not able to observe the conversion of the distorted higher energy G-pep• radical to a more stable planar conformation because the unsequestered G-pep• rapidly decays by solvent quenching as reaction times are increased beyond 10 s.

Remarkably, through careful use of time-resolved freeze-quench, thermal annealing, and temperature-dependent EPR spectroscopy, we were able to detect the elusive 5′-dAdo• radical along with G-pep• at intermediate quench times, thus allowing us to ask: is this free 5′-dAdo• radical indeed the catalytically active species formed subsequent to Ω that directly carries out the H-atom abstraction reaction? To test this, one would typically quench the reaction over a range of times and observe whether the loss of 5′-dAdo• and formation of G-pep• occur synchronously. Unfortunately, G-pep• is insufficiently stable in fluid solution, and it does not build up with longer quench times. We therefore employed a complementary approach: Monitoring 5′-dAdo• loss and G-pep• formation at low temperatures, where G-pep• is stable. During cryogenic annealing, we could then monitor the conversion of 5′-dAdo• to the G-pep• radical, stabilized in the frozen state. These cryoannealing measurements reveal the mechanistically direct conversion of the 5′-dAdo• to the G-pep• glycyl radical.

The present results provide the first direct observation of the 5′-dAdo• radical caught in the act of carrying out an H-atom abstraction from substrate. In doing so, they further provide new insights into the mechanistic steps by which the members of the large superfamily of RS enzymes carry out radical initiation. As visualized in Fig. 1 and observed here and previously, the first intermediate observed upon reaction of enzyme with SAM and substrate is an organometallic intermediate Ω, in which SAM has undergone

reductive cleavage of the S–C5′ bond to yield a $[4Fe–4S]^{3+}$ cluster that has the adenosyl 5′-C directly bound to its unique iron. This organometallic intermediate undergoes Fe–C5′ bond homolysis to liberate the 5′-dAdo• radical, which the current work reveals to be observable at longer quench times as a well-defined intermediate that is carefully chaperoned within the active site, rather than a highly reactive transition state-like species. As long imagined, but never before observed, this 5′-dAdo• then directly abstracts a hydrogen atom from substrate, forming the substrate G-pep• radical.

Materials and Methods

All reagents were purchased from MilliporeSigma at the highest available purity unless otherwise noted. 5′,5″,4′,3′-D_4-adenosine 5′-triphosphate salt solution were purchased from Cambridge Isotope Laboratories, Inc. Sodium dithionite and 99.8% D_2O was obtained from Acros Organics. Tris (hydroxymethyl) aminomethane (Trism) was purchased from Research Products International. The peptides (RVSGYAV, RVS(D_2-G)YAV, and RVS(I-A)YAV, purity ≥ 98%, N-term: free amine and C-term: free acid) were obtained from Celtek peptides. All spectroscopy samples were prepared under an anaerobic atmosphere in a mBraun glove box (O_2 < 8 ppm) or in a COY chamber (O_2 < 10 ppm).

Expression and Purification of PFL-AE. Expression and purification PFL-AE was carried out following a published protocol without modification (44).

Enzymatic SAM Synthesis. Natural abundant SAM and [adenosyl-5′,5″,4′,3′-D_4]-SAM were enzymatically synthesized using a clarified lysate of SAM synthase as previously described (64, 65). The purification of SAM was carried out following a previously published protocol (64).

EPR Sample Preparation. At room temperature, a solution of PFL-AE was reduced with sodium dithionite for 8 min before it was added to a solution of peptide and SAM in an X-band EPR tube (Wilmad LabGlass, 4 mm OD). The resulting mixture of these solutions yielded a sample with the following concentrations: 225 μM PFL-AE, 385 μM peptide, 6.75 mM sodium dithionite, 2.25 mM SAM in buffer (50 mM Tris-Cl, pH 8.5, 100 mM KCl, 10% glycerol). The samples were flash-frozen in liquid nitrogen at the indicated times after mixing.

RFQ Sample Preparation. RFQ experiments were performed using a protocol previously described in order to protect the protein from oxygen despite the RFQ instrument not being placed in an anaerobic environment (42, 44). A solution of PFL-AE was reduced with sodium dithionite for 8 min before it was loaded into one loop while the G-pep and SAM mixture was loaded into the other loop, achieving a post-mixing ratio of 1:1.7 of PFL-AE: G-pep. The mixing of these solutions yielded a sample with the following concentrations: 225 μM PFL-AE, 385 μM G-pep, 6.75 mM sodium dithionite, 2.25 mM SAM in buffer (50 mM Tris-Cl pH 8.5, 100 mM KCl, 10% glycerol). The sample loops were connected to a System 100 apparatus from Update Instrument and rapidly mixed. The mixture was quenched by spraying onto two rotating aluminum-coated copper wheels cooled in liquid nitrogen, at mixing time 1 s. The frozen powder was collected in a funnel and packed into precision Q-band tubes (2.5 mm OD) for X-band EPR analysis.

Continuous Wave (CW) EPR Spectroscopy. X-band CW spectroscopy on freeze-quenched samples was conducted at Montana State University using a Bruker EMX EPR spectrometer equipped with a Bruker/Cold Edge (Sumitomo Cryogenics) 10 K waveguide cryogen free system with an Oxford MercuryiTC controller unit and helium Stinger recirculating unit (Sumitomo Cryogenics, ColdEdge Technologies). The spin concentration of 5′-dAdo• and G-pep• present at 10 s was determined by comparison of the double integral of the EPR intensity to that of a standard curve made from solutions of 4.73 μM to 94.6 μM TEMPO radical in DI H_2O. X-band CW EPR spectroscopy performed on the RFQ samples was conducted at Northwestern University using a Bruker ESP 300 spectrometer equipped with an Oxford Instruments ESR 910 continuous helium flow cryostat. Simulations of experimental spectra were performed using EasySpin 5.2.30 (55) within the Matlab R2020b software suite (The Mathworks Inc.).

DFT Calculations. All DFT computations were carried out with the ORCA 4.2.1 software package (66–68). A simplified model for the G-pep• was generated by truncating the peptide between the Cα and N of Ser733 and between N and Cα of Tyr735 (*SI Appendix*, Fig. S1). The initial geometry for this simplified model was taken from the crystallographically determined structure of the RVSGYAV peptide bound to PFL-AE (PDB 3CB8) (36). The geometry around the Gly734 Cα was changed to a planar sp^2 radical configuration. In a constrained geometry optimization, the nonhydrogen atoms in the peptide fragment were fixed to the crystallographically determined geometry unless noted. The constrained geometry initially held the dihedral angle between the Cα–N and the Cα–H at 40°. This angle then was stepped by 5° until the calculated hyperfine tensors yielded the best match to those experimentally found. In this optimized conformation the dihedral angle between the Cα–N and the Cα–H bonds is 30°, which implies that the dihedral angle between the Cα–N and the 2pπ orbital of the Cα is 60°. Geometry optimization calculations utilized the B3LYP/G hybrid functional (69–71) and the Ahlrichs' valence triple-ξ with a polarization function basis set (72, 73). These input coordinates were also used in calculations using Becke's functional for exchange along with Perdew's functional for correlation (BP86) for comparison (69, 71). Hyperfine and *g*-tensors were calculated for all the input geometries by the coupled−perturbed self-consistent field approach using the B3LYP and BP86 hybrid functionals and EPR-III basis set (74, 75) in combination with an accurate spin−orbit coupling operator [RI-SOMF(1X)] (76). The isosurface plot presented below of the calculated HOMO (yellow) uses an isodensity of 0.20 au and was visualized as Gaussian cubes in Chemcraft 1.8 (77).

Data, Materials, and Software Availability. All study data are included in the article and/or *SI Appendix*.

ACKNOWLEDGMENTS. J.B.B. thanks the NIH (GM131889) for support. B.M.H. thanks the NIH (2 R01 GM111097), and also the NSF (MCB-1908587), for support. M.N.L. (F32GM140713) was supported by the NIH.

1. R. J. P. Williams, The necessary and the desirable production of radicals in biology. *Phil. Trans. R. Soc. Lond. B* **311**, 593–603 (1985).
2. J. Stubbe, Radicals in biological catalysis. *Biochemistry* **27**, 3893–3900 (1988).
3. P. A. Frey, Importance of organic radicals in enzymatic cleavage of unactivated C-H bonds. *Chem. Rev.* **90**, 1343–1357 (1990).
4. N. Oberg, T. W. Precord, D. A. Mitchell, J. A. Gerlt, RadicalSAM.org: A resource to interpret sequence-function space and discover new radical SAM chemistry. *ACS Bio. Med. Chem. Au* **2**, 22–35 (2022).
5. H. J. Sofia, G. Chen, B. G. Hetzler, J. F. Reyes-Spindola, N. E. Miller, Radical SAM, a novel protein superfamily linking unresolved steps in familiar biosynthetic pathways with radical mechanisms: Functional characterization using new analysis and information visualization methods. *Nucleic Acids Res.* **29**, 1097–1106 (2001).
6. J. B. Broderick, B. R. Duffus, K. S. Duschene, E. M. Shepard, Radical S-adenosylmethionine enzymes. *Chem. Rev.* **114**, 4229–4317 (2014).
7. P. A. Frey, A. D. Hegeman, F. J. Ruzicka, The radical SAM superfamily. *Crit. Rev. Biochem. Mol. Biol.* **43**, 63–88 (2008).
8. B. J. Landgraf, E. L. McCarthy, S. J. Booker, Radical S-adenosylmethionine enzymes in human health and disease. *Annu. Rev. Biochem.* **85**, 485–514 (2016).
9. G. L. Holliday *et al.*, Atlas of the radical SAM superfamily: Divergent evolution of function using a "Plug and Play" domain. *Methods Enzymol.* **606**, 1–71 (2018).
10. Y. Nicolet, Structure-function relationships of radical of radical SAM enzymes. *Nat. Catal.* **3**, 337–2020 (2020).
11. J. L. Vey, C. L. Drennan, Structural insights into radical generation by the radical SAM superfamily. *Chem. Rev.* **111**, 2487–2506 (2011).
12. C. J. Walsby, D. Ortillo, W. E. Broderick, J. B. Broderick, B. M. Hoffman, An anchoring role for FeS Clusters: Chelation of the amino acid moiety of S-adenosylmethionine to the unique iron site of the [4Fe-4S] cluster of pyruvate formate-lyase activating enzyme. *J. Am. Chem. Soc.* **124**, 11270–11271 (2002).
13. C. Krebs, W. E. Broderick, T. F. Henshaw, J. B. Broderick, B. H. Huynh, Coordination of adenosylmethionine to a unique iron site of the [4Fe-4S] of pyruvate formate-lyase activating enzyme: A Mössbauer spectroscopic study. *J. Am. Chem. Soc.* **124**, 912–913 (2002).
14. C. J. Walsby *et al.*, Electron-nuclear double resonance spectroscopic evidence that S-adenosylmethionine binds in contact with the catalytically active $[4Fe-4S]^+$ cluster of pyruvate formate-lyase activating enzyme. *J. Am. Chem. Soc.* **124**, 3143–3151 (2002).
15. C. J. Walsby *et al.*, Spectroscopic approaches to elucidating novel iron-sulfur chemistry in the "Radical SAM" protein superfamily. *Inorg. Chem.* **44**, 727–741 (2005).
16. W. E. Broderick, B. M. Hoffman, J. B. Broderick, Mechanism of radical initiation in the radical S-adenosyl-l-methionine superfamily. *Acc. Chem. Res.* **51**, 2611–2619 (2018).
17. J. B. Broderick, W. E. Broderick, B. M. Hoffman, Radical SAM enzymes: Nature's choice for radical reactions. *FEBS Lett.* **597**, 92–101 (2023).
18. B. M. Hoffman, W. E. Broderick, J. B. Broderick, Mechanism of radical initiation in the radical SAM enzyme superfamily. *Annu. Rev. Biochem.* **92**, 333–349 (2023).
19. K. A. Shisler, J. B. Broderick, Glycyl radical activating enzymes: Structure, mechanism, and substrate interactions. *Arch. Biochem. Biophys.* **546**, 64–71 (2014).

20. T. Selmer, A. J. Pierik, J. Heider, New glycyl radical enzymes catalysing key metabolic steps in anaerobic bacteria. *Biol. Chem.* **386**, 981–988 (2005).
21. S. Craciun, E. P. Balskus, Microbial conversion of choline to trimethylamine requires a glycyl radical enzyme. *Proc. Natl. Acad. Sci. U.S.A.* **109**, 21307–21312 (2012).
22. B. J. Levin *et al.*, A prominent glycyl radical enzyme in human gut microbiomes metabolizes trans-4-hydroxy-L-proline. *Science* **355**, eaai8386 (2017).
23. D. Liu *et al.*, Indoleacetate decarboxylase is a glycyl radical enzyme catalysing the formation of malodorant skatole. *Nat. Commun.* **9**, 4224 (2018).
24. S. C. Peck *et al.*, A glycyl radical enzyme enables hydrogen sulfide production by the human intestinal bacterium Bilophila wadsworthia. *Proc. Natl. Acad. Sci. U. S. A.* **116**, 317103176 (2019).
25. A. F. V. Wagner, M. Frey, F. A. Neugebauer, W. Schäfer, J. Knappe, The free radical in pyruvate formate-lyase is located on glycine-734. *Proc. Natl. Acad. Sci. USA* **89**, 996–1000 (1992).
26. J. Knappe, G. Sawers, A radical-chemical route to acetyl-CoA: The anaerobically induced pyruvate formate-lyase system of Escherichia coli. *FEMS Microbiol. Rev.* **75**, 383–398 (1990).
27. J. Knappe, H. P. Blaschkowski, P. Gröbner, T. Schmitt, Pyruvate formate-lyase of *Escherichia coli*: The acetyl-enzyme intermediate. *Eur. J. Biochem.* **50**, 253–263 (1974).
28. J. Knappe, F. Neugebauer, A. H. P. Blaschkowski, M. Gänzler, Post-translational activation introduces a free radical into pyruvate formate-lyase. *Proc. Natl. Acad. Sci U.S.A.* **81**, 1332–1335 (1984).
29. M. Frey, M. Rothe, A. F. V. Wagner, J. Knappe, Adenosylmethionine-dependent synthesis of the glycyl radical in pyruvate formate-lyase by abstraction of the glycine C-2 pro-S hydrogen atom. *J. Biol. Chem.* **269**, 12432–12437 (1994).
30. M. R. Nnyepi, Y. Peng, J. B. Broderick, Inactivation of *E. coli* pyruvate formate-lyase: Role of AdhE and small molecules. *Arch. Biochem. Biophys.* **459**, 1–9 (2007).
31. A. Becker *et al.*, Structure and mechanism of the glycyl radical enzyme pyruvate formate-lyase. *Nat. Struct. Biol.* **6**, 969–975 (1999).
32. Y. Peng, S. E. Veneziano, G. D. Gillispie, J. B. Broderick, Pyruvate formate-lyase, Evidence for an open conformation favored in the presence of its activating enzyme. *J. Biol. Chem.* **285**, 27224–27231 (2010).
33. A. F. V. Wagner *et al.*, YfiD of Escherichia coli and Y061 of bacteriophage T4 as autonomous glycyl radical cofactors reconstituting the catalytic center of oxygen-fragmented pyruvate formate-lyase. *Biochem. Biophys. Res. Commun.* **285**, 456–462 (2001).
34. S. E. J. Bowman *et al.*, Solution structure and biochemical characterization of a spare part protein that restores activity to an oxygen-damaged glycyl radical enzyme. *J. Biol. Inorg. Chem.* **24**, 817–829 (2019).
35. M. C. Andorfer, L. R. F. Backman, P. L. Li, E. C. Ulrich, C. L. Drennan, Rescuing activity of oxygen-damaged pyruvate formate-lyase by a spare part protein. *J. Biol. Chem.* **297**, 101423 (2021).
36. J. L. Vey *et al.*, Structural basis for glycyl radical formation by pyruvate formate-lyase activating enzyme. *Proc. Natl. Acad. Sci. U.S.A.* **105**, 16137–16141 (2008).
37. K. A. Shisler *et al.*, Monovalent cation activation of the radical SAM enzyme pyruvate formate-lyase activating enzyme. *J. Am. Chem. Soc.* **139**, 11803–11813 (2017).
38. T. F. Henshaw, J. Cheek, J. B. Broderick, The $[4Fe\text{-}4S]^{+}$ cluster of pyruvate formate-lyase activating enzyme generates the glycyl radical on pyruvate formate-lyase: EPR-detected single turnover *J. Am. Chem. Soc.* **122**, 8331–8332 (2000).
39. J. Cheek, J. B. Broderick, Adenosylmethionine-dependent iron-sulfur enzymes: Versatile clusters in a radical new role. *J. Biol. Inorg. Chem.* **6**, 209–226 (2001).
40. J. M. Buis, J. B. Broderick, Pyruvate formate-lyase activating enzyme: Elucidation of a novel mechanism for glycyl radical formation. *Arch. Biochem. Biophys.* **433**, 288–296 (2005).
41. S. C. Wang, P. A. Frey, S-adenosylmethionine as an oxidant: The radical SAM superfamily. *Trends Biochem. Sci.* **32**, 101–110 (2007).
42. M. Horitani *et al.*, Radical SAM catalysis via an organometallic intermediate with an Fe-[5′-C]-deoxyadenosyl bond. *Science* **352**, 822–825 (2016).
43. R. J. Jodts *et al.*, Computational description of alkylated iron-sulfur organometallic clusters. *J. Am. Chem. Soc.* **145**, 13879–13887 (2023).
44. A. S. Byer *et al.*, Paradigm shift for radical S-adenosyl-L-methionine reactions: The organometallic intermediate **Ω** is central to catalysis. *J. Am. Chem. Soc.* **140**, 8634–8638 (2018).
45. K. H. Ebrahimi *et al.*, The radical-SAM enzyme viperin catalyzes reductive addition of a 5′-deoxyadenosyl radical to UDP-glucose in vitro. *FEBS Lett.* **591**, 2394–2405 (2017).
46. A. Pagnier *et al.*, Radical SAM enzyme spore photoproduct lyase: Properties of the W organometallic interrmediate and identification of stable protein radicals formed during substrate-free turnover. *J. Am. Chem. Soc.* **142**, 18652–18660 (2020).
47. A. R. Balo *et al.*, Trapping a cross-linked lysine-tryptophan radical in the catalytic cycle of the radical SAM enzyme SuiB. *Proc. Natl. Acad. Sci. U. S. A.* **118**, e2101571118 (2021).
48. W. D. Robertson, K. Warncke, Photolysis of adenosylcobalamin and radical pair recombination in ethanolamine ammonia-lyase probed on the micro- to millisecond time scale by using time-resolved optical absorption spectroscopy. *Biochemistry* **48**, 140–147 (2009).
49. H. Yang *et al.*, The elusive 5′-deoxyadenosyl radical: Captured and characterized by electron paramagnetic resonance and electron nuclear double resonance spectroscopies. *J. Am. Chem. Soc.* **141**, 12139–12146 (2019).
50. H. Yang *et al.*, Photoinduced electron transfer in a radical SAM enzyme generates an S-adenosylmethionine derived methyl radical. *J. Am. Chem. Soc.* **141**, 16117–16124 (2019).
51. S. Impano *et al.*, Active-site controlled, jahn-teller enabled regioselectivity in reductive S-C bond cleavage of S-adenosylmethionine (SAM) in radical-SAM enzymes. *J. Am. Chem. Soc.* **143**, 335–348 (2021).
52. S. Impano *et al.*, S-Adenosyl-L-ethionine is a catalytically competent analog of S-adenosyl-l-methionine (SAM) in the radical SAM enzyme HydG. *Angew. Chem. Int. Ed.* **60**, 4666–4672 (2021).
53. R. I. Sayler *et al.*, Trapping and electron paramagnetic resonance characterization of the 5′-dAdo• radical in a radical S-adenosylmethionine enzyme reaction with a non-native substrate. *ACS Cent. Sci.* **5**, 1777–1785 (2019).
54. M. N. Lundahl *et al.*, Mechanism of radical S-adenosyl-L-methionine adenosylation: Radical intermediates and the catalytic competence of the 5′-deoxyadenosyl radical. *J. Am. Chem. Soc.* **144**, 5087–5098 (2022).
55. S. Stoll, A. Schweiger, EasySpin, a comprehensive software package for spectral simulation and analysis in EPR. *J. Magn. Res.* **178**, 42–55 (2006).
56. A. McSkimming, A. Sridharan, N. B. Thompson, P. Müller, D. L. M. Suess, An [Fe4S4]3+-alkyl cluster stabilized by an expanded scorpionate ligand *J. Am. Chem. Soc.* **142**, 14314–14323 (2020).
57. M. B. Ho *et al.*, Characterization by ENDOR spectroscopy of the iron-alkyl bond in a synthetic counterpart of organometallic intermediates in radical SAM enzymes. *J. Am. Chem. Soc.* **144**, 17642–17659 (2022).
58. V. Barone, C. Adamo, A. Grand, M. Fontecave, R. Subra, Conformational behavior and magnetic properties of organic radicals derived from amino acid residues. The dipeptide analog of glycine radical. *J. Am. Chem. Soc.* **117**, 1083–1089 (1995).
59. C. Duboc-Toia *et al.*, Very high-field EPR study of glycyl radical enzymes. *J. Am. Chem. Soc.* **125**, 38–39 (2003).
60. J. Knappe *et al.*, Pyruvate formate-lyase reaction in *Escherichia coli*. The enzymatic system converting an inactive form of the lyase into the catalytically active enzyme. *Eur. J. Biochem.* **11**, 316–327 (1969).
61. H. Conradt, M. Hohmann-Berger, H.-P. Hohmann, H. P. Blaschkowski, J. Knappe, Pyruvate formate-lyase (inactive form) and pyruvate formate-lyase activating enzyme of *Escherichia coli*: Isolation and structural properties. *Arch. Biochem. Biophys.* **228**, 133–142 (1984).
62. V. Unkrig, F. A. Neugebauer, J. Knappe, The free radical of pyruvate formate-lyase. Characterization by EPR spectroscopy and involvement in catalysis as studied with the substrate-analogue hypophosphite. *Eur. J. Biochem.* **184**, 723–728 (1989).
63. A. Becker, W. Kabsch, X-ray structure of pyruvate formate-lyase in complex with pyruvate and CoA. *J. Biol. Chem.* **277**, 40036–40042 (2002).
64. A. S. Byer, E. C. McDaniel, S. Impano, W. E. Broderick, J. B. Broderick, Mechanistic studies of radical SAM enzymes: Pyruvate formate-lyase activating enzyme and lysine 2,3-aminomutase case studies. *Methods Enzymol.* **606**, 269–318 (2018).
65. W. G. Walls *et al.*, The B12-independent glycerol dehydratase activating enzyme from *Clostridium butyricum* cleaves SAM to produce 5′-deoxyadenosine and not 5′-deoxy-5′-(methylthio) adenosine. *J. Inorg. Biochem.* **227**, 111662 (2021).
66. F. Neese, The ORCA program system. *Comput. Mol. Sci.* **2**, 73–78 (2012).
67. E. F. Valeev, Libint: A library for the evaluation of molecular integrals of many-body operators over Gaussian functions. Version 2.6.0. http://libint.valeyev.net/. (2019).
68. S. Lehtola, C. Steigemann, M. J. T. Oliveira, M. A. L. Marques, Recent developments in libxc–A comprehensive library of functionals for density functional theory. *SoftwareX* **7**, 1–5 (2018).
69. A. D. Becke, Density-functional exchange-energy approximation with correct asymptotic behavior. *Phys. Rev. A* **38**, 3098–3100 (1988).
70. C. Lee, W. Yang, R. G. Parr, Development of the Colle-Salvetti correlation energy formula into a functional of the electron density. *Phys. Rev. B Condens. Matter* **37**, 785–789 (1988).
71. J. P. Perdew, Density-functional approximation for the correlation-energy of the inhomogeneous electron-gas. *Phys. Rev. B* **33**, 8822–8824 (1986).
72. F. Weigend, R. Ahlrichs, Balanced basis sets of split valence, triple zeta valence and quadruple zeta valence quality for H to Rn: Design and assessment of accuracy. *J. Chem. Phys.* **7**, 3297–3305 (2005).
73. F. Weigend, Accurate Coulomb-fitting basis sets for H to Rn. *Phys. Chem. Chem. Phys.* **8**, 1057–1065 (2006).
74. V. Barone, *Recent Advances in Density Functional Methods* (World Scientific, Singapore, 1995), p. 287.
75. V. Barone, M. Cossi, J. Tomasi, A new definition of cavities for the computation of solvation free energies by the polarizable continuum model. *J. Chem. Phys.* **107**, 3210–3221 (1997).
76. F. Neese, Efficient and accurate approximations to the molecular spin-orbit coupling operator and their use in molecular g-tensor calculations. *J. Chem. Phys.* **122**, 034107 (2005).
77. G. A. Zhurko, Chemcraft - graphical program for visualization of quantum chemistry computations (Version 1.8, Build 654, Ivanovo, Russia, 2005). https://chemcraftprog.com. Accessed 23 February 2022.